RSC Advances

ROYAL SOCIETY OF CHEMISTRY

www.rsc.org/advances

1/14/2016

Fluid Flow Analysis of Continuous and Segmented Riblet Structures

Samuel Martin and Bharat Bhushan[1]
Nanoprobe Laboratory for Bio & Nanotechnology and Biomimetics (NLBB)
The Ohio State University
201 W. 19th Avenue, Columbus, Ohio 43210-1142, USA

Abstract

The scales of fast-swimming sharks contain riblet structures with microgrooves, aligned in the direction of fluid flow, that result in water moving efficiently over the surface. In previous experimental and modeling studies, it has been shown that riblet structures provide a drag reduction by lifting the vortices formed in turbulent flow that generate transverse shear stresses. Drag reductions on the order of 10% when compared to a smooth, flat surface have been reported. Most experimental and modeling work has analyzed continuous riblet configurations with some experimental work for segmented riblet configurations. To better understand the role of vortices on drag reduction, various continuous and segmented, blade riblet geometries and their vortex structures were studied and compared with that for a flat surface. To understand the role of various segmented riblet designs, various shark-skin-inspired riblet structures were created in which riblet gaps and offsets were independently modified. Through this work, optimal riblet dimensions of spacing, height, thickness, gap, and offset were determined. A better understanding of riblet design for drag allows for the fabrication of drag-reducing surfaces in marine, medical, and industrial applications utilizing features ranging from the micro- to nanoscale dependent upon the scale of the components.

Keywords:

Shark skin, drag, vortex, riblet, modeling, turbulence

[1] Corresponding author: bhushan.2@osu.edu

1. Introduction

Nature has evolved efficient and multi-purpose objects using commonly occurring materials. These objects have many applications that can aid humanity and can be of commercial interest. Mimicking these biological structures and using them for design inspirations is the field of biomimetics.[1,2] An inspiration for a drag reduction surface is provided by shark skin because fast-swimming sharks are able to move through water quickly with a low energy input.[3–7]

The skin of fast-swimming sharks has been a biomimetic motivation for the design of a low drag and anti-fouling surface.[5–7] These sharks can quickly and easily move through water and have scales called dermal denticles (little skin teeth) with riblets (microscopic grooves) aligned parallel to fluid flow as shown in **Fig. 1**. The scales are generally 0.2–0.5 mm in size with the grooves spaced 30–100 μm apart; however, the scale patterns differ between sharks and even depending on the scale location on a shark.[3,8] In **Fig. 1**, the Mako shark has scales with little gaps and no offsets[9] (referred to as aligned-segmented riblets), whereas the Spiny Dogfish has gaps and offsets[8] (referred to as staggered-segmented riblets).

The low drag and anti-fouling properties found in shark skin have wide applications due to the scalability of riblet dimensions. Riblets can be designed from the nanoscale to macroscale depending on the application. By choosing adequate riblet dimensions, these surfaces can decrease fuel consumption in the transportation industry by reducing viscous drag on vehicles, aircraft, or ships. Another application area is in the biomedical field. For example, in micro- and nanofluidic biosensors, drag reduction in micro- and nanochannels is important and nanoscale riblet structures may be of interest.[10] Shark-skin-inspired surfaces for aircraft applications have been studied by National Aeronautics and Space Administration (NASA)[11] and the German Aerospace Center.[5] In ships, these energy efficient surfaces were applied to the hulls of US boats in the 1984 Los Angeles Olympics and 1987 America's Cup. Furthermore, they have been incorporated into the Speedo FastSkin® swimsuit worn by Michael Phelps in the 2008 Beijing Olympics when setting records and winning gold medals. These suits had drag reduction effects of up to 4% in men and 3% in women,[12] and were subsequently outlawed by the International Swimming Federation (FINA) supposedly due to their drag reduction benefits derived unfairly by some swimmers.

In addition to low drag, these microstructured riblets are self-cleaning and help repel fouling of microbiological matter, such as bacteria or algae biofilms, as well as macrobiological

organisms, such as barnacles and muscles.[5–7] This self-cleaning occurs through various mechanisms such as increased surface fluid velocity and reduced microorganism attachment time due to surface geometry. Increased surface velocity makes it harder for matter to land and grow. Surfaces features smaller than the size of the microorganism or containing sharp edges reduce and deter microorganisms landing and settlement. Also, surface features larger than the size of microorganisms prevent landing and settlement on the entire surface and thus reduce the extent of biofouling.[13]

In order to study mechanisms of potential drag reduction, various riblet geometries and configurations have been studied through experiments in open and closed channel flow and modeling in closed channel flow. In closed channel experiments using continuous, sawtooth riblets, Walsh[14] and Rohr et al.[15] saw drag reductions of 8% in water and 9% in air, respectively. Using the so-called Berlin oil channel in open channel flow, Bechert et al.[5] studied sawtooth, scalloped, and blade geometries in the continuous configuration and showed that optimal blade geometry had the greatest drag reduction of 10% followed by scalloped and sawtooth at 7% and 5%, respectively. Staggered-segmented, blade riblet configurations were also studied using the Berlin oil channel in Bechert et al.[16] showing that these staggered-segmented configurations were inferior to continuous configurations. Jung and Bhushan[8] studied aligned-segmented, blade configurations in a closed channel flow and showed a 30% drag reduction in water calculated through a pressure drop (indicating drag reduction) using a differential manometer. Bixler and Bhushan[7,17] studied aligned-segmented blade, continuous blade, and continuous sawtooth configurations with oil, water, and air using a differential manometer. In oil, a 7% pressure drop was obtained with continuous and aligned-segmented, blade riblets. In water, a 34% pressure drop was obtained with aligned-segmented, blade riblets. In air, a 26% pressure drop was obtained with continuous, sawtooth riblets. Bixler and Bhushan[7] studied continuous, sawtooth riblets on airfoils showing a 14% drag reduction at a 6° angle of attack.

Through modeling of continuous and sawtooth geometries, Chu and Karniadakis,[18] Choi et al.,[19] and Goldstein et al.[20] have shown drag reductions of up to 3–6%. A drag reduction is formed by riblets lifting the streamwise vortices formed in turbulent flow that generate transverse shear stresses. Streamwise vortices are referred to as vortices traveling in the predominant flow direction and rotating along an axis line in the streamwise direction. In this drag reduction mechanism, riblets reduce the propensity of streamwise vortex formation in the

riblet valleys and inhibit spanwise motion of fluid caused by vortices.[18–20] In open channel flow experiments, Lee and Lee[21] compared vortices on a flat and riblet surface using a smoke-wire flow visualization technique with olive-oil atomized in air, shown in **Fig. 2**. On the riblet surface, the vortex is lifted away from the surface to create a drag reduction surface. These riblets have a non-dimensional spacing (s^+) of 25.2 and non-dimensional height (h^+) of 12.6 (s^+ and h^+ will be defined later).

In laminar flow where vortices are not generated, this method of drag reduction is not possible. Instead, a drag increase can result due to the greater riblet surface area.[20,22] In the transitional regime, a drag reduction is possible due to the possibility of vortex structures being created; however, a drag reduction through this mechanism is best obtained through fully turbulent flow.

Experimental and modeling studies have primarily researched various riblet geometries and configurations that lead to drag reductions and come up with the drag-reduction mechanism of riblets controlling the vortices generated in turbulent flow. With appropriately-sized riblets, these vortices are lifted away from the riblet surface decreasing the overall shear stress and therefore creating a surface that reduces drag. However when the riblets do not effectively lift the vortices from the surface, the overall surface can become a drag increasing case.[23] Based on experiments and modeling, optimal riblet geometries have shown on the order of 10% drag reduction with riblet dimensions $s^+ \approx 15 - 20$ and $h^+ \approx 8 - 10$.[5,14,23,24]

In order to compare various riblets designs, dimensions of the riblet geometry are commonly non-dimensionalized using

$$s^+ = sv_\tau/\nu \quad (1)$$

$$\text{and} \qquad v_\tau = (\tau_0/\rho)^{1/2} \quad (2)$$

and denoted by a superscript +.[5,14] In this equation, the distance between microgrooves is the riblet spacing where s is the dimensional riblet spacing, v_τ is the wall shear stress velocity, τ_0 is the wall shear stress, ρ as the density of the fluid, and ν is the kinematic viscosity of the fluid. The wall shear stress velocity is simply a quantity that has dimensions of velocity and is in a form that allows for different wall shear stresses to be compared.[25] Similarly, the height and thickness parameters can be non-dimensionalized through

$$h^+ = hv_\tau/\nu \quad (3)$$

$$t^+ = tv_\tau/\nu \quad (4)$$

respectively.[7]

An understanding of the size of streamwise vortices, such as diameter and streamwise length, and the interactions of vortices with different riblet geometry for continuous riblet configurations needs to be studied in order to better understand how vortices interact with riblet surfaces with different geometries. The wide variation of riblet designs in shark skin necessitates studying segmented configurations in order to better understand the drag reduction mechanism. Primarily, continuous configurations have been studied, but segmented configurations could lead to more insights into the mechanism. By undertaking a comprehensive study on the effect of the different parameters in segmented riblet geometries, these insights could be obtained. These results could help lead to better drag-reducing riblet designs for the various potential applications.

In this paper, a computational fluid dynamic (CFD) model of blade riblet structures in continuous, aligned-segmented, and staggered-segmented configurations in a closed channel flow was created in order to further study the effect of riblet geometry as well as dimensions of vortices on drag reduction. The gaps and offsets in the staggered configurations were independently changed, and the resulting drag and vortex formations were compared to each other as well as to a flat surface and continuous riblet configurations.

2. Vortex generation and dimensions background

The majority of this drag reduction research concerns streamwise vortices, and so, vortex generation and dimensions are reviewed in order to better understand the drag reduction mechanism of riblets. To start, fluid flow can be characterized as laminar, transitional, or turbulent. Laminar flow is steady with repeatable sequences occurring at Reynolds numbers less than approximately 2100 in closed channel flow. Turbulent flow has highly chaotic flow characteristics with irregular variations in time and space. Fully turbulent flow occurs at a Reynolds number of approximately 4000 in closed channel flow. Transitional flow occurs between these two Reynolds numbers with characteristics of laminar and turbulent flow. The transitional point occurs around 500,000 in open channel flow.[25]

In the turbulent regime, the kinetic energy from the free-stream flow is transformed into turbulent fluctuations and then dissipated into internal energy through viscous action.[25] The source for most of the turbulent kinetic-energy production in a boundary layer can be found in the wall region.[26] On the left axis of **Fig. 3**, the wall region or boundary layer region is

schematically shown. This region can be split up into the viscous sublayer, the buffer layer, and the log-law region of the inner layer. Outside of this region is commonly referred to as the outer region.[27,28]

The boundary layer regions are determined based on their non-dimensional distance from the wall using the wall shear stress velocity similarly to the velocity term in Reynolds number

$$y^+ = yv_\tau/\nu \quad (5)$$

where y^+ is the non-dimensional distance from the wall and y is the dimensional distance from the wall. In turbulent flow, the non-dimensional average velocity in the viscous sublayer is linear with the distance from the wall and in the log-law region is proportional to the logarithmic distance from that point to the wall. In the buffer region, neither profile is used and the curves are fitted together. These velocity profiles together are referred to as the law of the wall.[29] Non-dimensional velocity can be calculated as V/v_τ and is commonly referred to as u^+ in law of the wall terminology. The wall region is $y^+ \leq 100$ with the viscous sublayer at $0 \leq y^+ \leq 5$, the buffer layer at $5 \leq y^+ \leq 30$, and the log-law region of the inner layer at $30 \leq y^+ \leq 100$.[30]

The turbulent action found in the boundary layer leads to fluid structures that are called coherent structures. Various fluid structures, such as vortices, bursts, or sweeps, can be found depending on the region within the boundary layer. Vortices are regions of fluid where the flow is rotating along an axis line in a roughly circular or spiral pattern and can take the form of streamwise vortices or hairpin (also called arch or horseshoe) vortices. Bursts are ejections of low-speed fluid away from the wall, and sweeps are inrushes of high-speed fluid toward the wall.[31–33] Robinson[32] proposed an ideal schematic of the vortex structures in the different regions of the turbulent boundary layer where streamwise vortices dominate the buffer layer, hairpin vortices dominate in the outer region, and both exist in the log-law region where they overlap.

Figure 3 also shows potential streamwise vortex interactions located within the buffer layer on flat and riblet surfaces with the vortices traveling along the streamwise direction (*x*). The boundary layer and coherent structures have been studied through open surface water flows using hydrogen bubble streak markers and hot-wire anemometer measurements with dye injection at the wall,[34] hot-film sensor experiments,[35] wind tunnel experiments with the smoke-wire technique,[36] and computer simulations.[37,38] Through these techniques, the streamwise vortices have been found to be approximately at $y^+ = 20 - 30$ with diameter $d^+ \approx 30$ and quasi-periodic in the spanwise direction every $\Delta z^+ \approx 50$, where Δz^+ is the non-dimensional

spanwise spacing.[34–36,38,39] The streamwise vortices have a non-dimensional length of approximately 100–200 found through computer simulations[38] and direct numerical simulations.[40]

In **Fig. 3** on the flat surface, two streamwise vortices with a low-speed streak between the vortices are shown. These pairs of counter-rotating vortices repeat themselves with fluid rotation towards the surface or away from the surface. Between pairs of vortices rotating away from the surface and thus forcing fluid away from the surface, low-speed regions can be found every $\Delta z^+ \approx 100$.[35,36,39] This counter-rotating streamwise pair does not occur as often as a single streamwise vortex in the buffer and log-law regions.[28] As vortices rotate, they also translate in the cross-flow direction on the surface interacting with other vortices and the surface creating more bursting motions. The vortex translations, bursting motions, and chaotic flow are all forms of momentum transfer and factors in fluid drag.[27,41,42] They increase shear stress at the wall (τ_0) by increasing the velocity gradient ($\partial u/\partial y$) in the fluid shear stress equation given by

$$\tau_0 = \mu \left.\frac{\partial u}{\partial y}\right|_{y=0} \tag{6}$$

where μ is the dynamic viscosity and can be derived from $\mu = \rho\nu$.

Because vortices increase the velocity gradient at the wall and therefore produce transverse shear stress leading to higher drag. Therefore, controlling these vortices helps in creating low drag surfaces. The riblets on the scales of fast-swimming sharks help control the streamwise vortices in turbulent fluid flow by lifting the vortices from the surface as shown in **Fig. 3** on the riblet surface. As vortices are lifted from the surface, bursting and sweeping motions, where high-velocity fluid mixes with low-velocity fluid near the surface, are decreased. The shear stress at the riblet peaks increases; however, the shear stress in the riblet valleys decreases. Due to the much greater surface area in the riblet valleys, an overall lower drag surface is obtained when compared to a flat surface. On the flat surface, vortices create many zones of high shear stress across the entire surface.[23]

3. Simulation approach

In this section, the CFD program and turbulence model will be presented, followed by the model set-up, spatial discretization, and the riblet geometry models. This simulation was set-up for closed channel to directly compare a flat and riblet surface. For completeness, an open channel set-up could be modeled through a symmetric boundary condition at the opposite surface

to the riblet surface. Similar results can be expected for open channel due to similar vortex generation in turbulent flow.

These simulations were run on the Glenn supercomputer using four cores with 12 processors each at the Ohio Supercomputer Center.[43] Each simulation took approximately one week to reach the time-averaging state for fully turbulent flow and approximately one additional week was required to complete the time averaging portion of the simulation due to the transient state.

A transient solution was chosen over a steady state one due to the chaotic nature of the turbulent flow. By using a transient solution, the vortices interacting with the riblet and flat surfaces could be analyzed and compared at discrete time steps in order to further understand the drag reduction mechanism.

3.1. CFD program

To simulate fluid flow over riblets, the CFD software package ANSYS Fluent 14.5 was used which uses the finite volume method to solve the governing equations which include the momentum Navier-Stokes and continuity equations. This robust commercial package contains various turbulence models that have been used in many studies. The package can implement parallel processing and includes solver improvements such as solving the momentum and pressure-based continuity equations in a coupled manner. These features accelerate convergence and reduce solution time.[44]

The large-eddy simulation (LES) and direct numerical simulation (DNS) are two turbulence models that have been used to study riblets in fluid flow.[45] In LES, the large scales of the flow field are resolved whereas the small scales of the flow field are filtered out based on the turbulence criteria. This modeling results in greater accuracy than other Fluent models such as the Reynolds-averaged Navier Stokes models. In LES, a subgrid-scale (SGS) is chosen to model the unresolved small scale fluid motions. In DNS, all the flow scales are resolved for the entire spatial and temporal scales. By solving the equations at all scales, the greatest accuracy is obtained; however, a very fine mesh must be used in order to resolve the fluid flow down to the smallest dissipative scales and therefore a huge computational expense is required.

Due to the computational requirement for DNS, which would have severely limited the number of test cases even at low turbulent Reynolds numbers, LES was chosen as the turbulence model. Because LES filters out the small scales, the computational expense is decreased

allowing for a parametric study. This filtering affects the results, but the small scales play a smaller role in the process of transporting mass and energy when compared to the large scales which play a greater role in drag change in riblets.

The mesh size and time step were chosen to resolve the large scales with the SGS filtering out the small scales. In this work, the Smagorinsky-Lilly SGS was chosen which assumes that the small scale energy production and dissipation are in equilibrium. Several different SGS approaches to filter small scales were tested and compared to fit the law of the wall to best decide which SGS to choose.[44]

3.2. Model set-up

Figure 4a shows the model design where the x, y, and z axes denote the streamwise, wall-normal, and spanwise directions, respectively. Similarly to y^+ in Eq. 5, x^+ and z^+ are non-dimensional parameters. The height, width, and length of the model are H, W, and L, respectively. The riblet surface is on the bottom wall and the flat surface is on the top wall, both prescribed with no-slip boundary conditions. The inlet and outlet surfaces and the left and right surfaces were prescribed with periodic boundary conditions so that wall effects would not interfere with the results. This closed channel model design allows for the flat and riblet surfaces to be directly compared for drag and vortex measurements.

In the streamwise direction, a constant instantaneous volume flux boundary condition was applied,

$$Q = \int V \, \mathrm{d}A_C = \frac{2}{3} A_C V_l \tag{7}$$

where $A_c = HW$ is the cross-sectional area, V is the average velocity in the streamwise direction, and V_l is the centerline velocity of a laminar profile with the same volume flux. In Eq. 7, V_l is 2/3 of V because of the difference between average and maximum velocity in closed channel flows.[25] The Reynolds number was calculated using

$$Re = V_l \delta / \nu \tag{8}$$

where $\delta = H/2$ is the channel half-width.[19]

The solution was initialized with a laminar velocity profile and turbulence fluctuations were added afterwards. The simulation was advanced until natural turbulence was developed by monitoring wall-shear stresses for quasi-periodic behavior upon which the simulation was continued for additional time to time average the results. The simulation had a computational

time step of $\Delta T V_l/\delta = 0.05$, where ΔT is the dimensional time step. The time averaging period was at least 500 non-dimensional time steps (T^+) where $T^+ = TV_l/\delta$. After averaging the drag over $T^+ = 500$ on a plane channel flow, the drag on the walls differed by $\pm 2\%$ of each other which agreed with the results by Walsh[14] and Choi et al.[19]

The various configurations that were analyzed are shown in **Figure 4b** which include the continuous; aligned-segmented; and staggered-segmented configurations. In the segmented configurations, the spacing, height, and thickness parameters were kept constant and only the lengths, gaps, and offsets of the riblet were modified for drag and vortex comparison.

To compare drag, the difference between the time-averaged drag on the riblet and flat surface was divided by the time-averaged drag on the flat surface to calculate the percentage drag change. To compare vortices, *y*-*z* planes with vorticity contours and tangential velocity vectors were plotted and the height, width, diameter, and distance from the wall for the vortices in the buffer layer were measured on the riblet and smooth surfaces. These definitions of various vortex dimensions are shown schematically in **Fig. 4c**.

3.3. Spatial discretization

The computational domain dimensions were chosen to be large enough to include the expected scales of the flow structures and to be greater than the minimal flow unit (100 non-dimensional units in the spanwise direction and 300 non-dimensional units in the streamwise direction where the length is non-dimensionalized similar to Eq. 1 using the spanwise or streamwise distance as the respective length scale) as determined by Jimenez and Moin.[46] For the continuous models, the height *H* and width *W* remained constant at 0.02 m which corresponded to 206 non-dimensional units in the smallest case. For the segmented models, the height *H* and width *W* remained constant at 0.015 m and 0.02 m which corresponded to approximately 250 and 333 non-dimensional units, respectively.

For the continuous models, the length *L* changed for the cases to keep a structured grid spacing at $x^+ \approx 35$ and with 16 nodes this corresponded to approximately 560 non-dimensional units. In the spanwise direction, the z^+ grid spacing was between 0.4–2.0 with $z^+ \approx 0.7$ for most cases. In the wall normal direction, there were 128 grid points with the first grid point on the smooth surface baseline case at $y^+ = 0.16$. Based on these inputs, the total number of hexahedral cells was around one million. For the segmented models, the length *L* changed for the cases in order to keep the periodic riblet pattern intact. In most cases, the length was 0.025 m

which corresponded to approximately 415 non-dimensional units. An unstructured, tetrahedral mesh was used in order to mesh the various segmented riblet designs. The mesh was controlled with at least 150 grid points in the wall-normal direction, and the first grid point on the smooth surface at $y^+ = 0.38$. In the spanwise direction, at least 165 grid points were used with an approximate z^+ grid spacing of 1.5. In the spanwise direction, at least 250 grid points were used with an approximate x^+ grid spacing of 1. Based on these inputs, the total number of tetrahedral cells was around four million.

In all models, the mesh was biased toward the riblets and flat surface in order to keep the first grid point below $y^+ = 1$ for all cases as required by the LES model and to more accurately resolve the flow near the walls. The grid resolution was kept the same on the smooth and riblet surfaces for drag comparison purposes and was much finer than the recommended requirements of $x^+ = 40$ and $z^+ = 20$ suggested by Anonymous.[44]

To validate the simulation, the non-dimensional mean streamwise velocity profile over a flat surface was compared to Spalding's law of the wall, shown in **Fig. 5**.[29] The dashed lines refer to the linear law and the log-law with the log-law formulation of $V/v_\tau = 2.5 \ln y^+ + 5.5$. The dotted line refers to Spalding's law of the wall, and the solid line refers to the present study. The law of the wall and the present LES simulation are in good agreement, which validates the simulation.

3.4. Riblet geometry models

The continuous riblet cases had two fluid parameters (velocity V and viscosity ν) and three riblet parameters (spacing s, height h, and thickness t) independently changed. These cases are presented in **Table 1**. In the table, the dimensional parameters are listed on the left and the resulting non-dimensional parameters are listed on the right.

The values of the dimensional parameters were chosen to fulfill several requirements. First, the dimensional parameters were chosen so that the cases would cover a wide non-dimensionalized range for the parameter. In addition, the values were chosen so that s^+ of 15–20 would be in the parameter's ranges. This range has been shown for optimal drag reduction. By centering the data on this range, it would allow for test cases on either side of this range to be investigated.

Additionally, the velocity and viscosity values were selected to show the non-dimensionalizing method is valid. By modifying the dimensional parameters and getting similar

changes in drag for their non-dimensional parameters, it shows that only the non-dimensional values are important and any parameter in the equation can be modified.

To better understand the relationship between riblet height and drag, two sets of riblet height cases were created. In the first set, only the height was modified with the other parameters matching the baseline case. In the second set, all of the parameters were modified to increase the Reynolds number, center s^+ near 23, and h^+ near 10.

These continuous riblet cases were compared to the segmented riblet cases in which the length of each riblet (L_1), the gap between the riblets (L_2), and the offset between riblets (L_3) were independently changed. These cases are presented in **Table 2**. In the table, the dimensional and non-dimensional parameters for the riblet geometry are listed at the top. To obtain $\nu/V_l = 2.4\ \mu m$, $\nu = 1 \times 10^{-6}\ m^2 s^{-1}$ was assumed, representative of water. The dimensional values for the segmented geometries are shown on the left, and the resulting non-dimensional values are shown on the right. The lengths were non-dimensionalized similar to Eq. 1 as $L_1^+ = L_1 v_\tau/\nu$, $L_2^+ = L_2 v_\tau/\nu$, and $L_3^+ = L_3 v_\tau/\nu$, respectively. The dimensional numbers for the various parameters were scaled up from actual riblet dimensions due to limitations with ANSYS Fluent when working with small numbers. Even with double precision, rounding errors could accumulate if actual riblet dimensions were used. Scaling up the numbers does not affect the results since only non-dimensional numbers affect the results, and this conclusion will be presented later.

In the segmented riblet cases, the spacing ($s^+ \approx 16$), height ($h^+ \approx 8$), thickness ($t^+ \approx 0.3$), and Reynolds number ($Re = 4180$) were kept constant. These cases were compared to the continuous case with these same riblet parameters showing a 9% drag reduction. In the aligned-segmented test cases, the length of each riblet (L_1) was varied from 2–6 times the length of the gap between riblets (L_2) because these ratios can be seen in shark scales. Also in the aligned-segmented test cases, the gap between the riblets (L_2) ranged from 0.25–2.35 times the length of each riblet (L_1) in order to get a wide range of non-dimensional riblet gaps. This wide range was necessary in order to examine streamwise vortices because they have a great effect on drag in riblets. In the staggered-segmented test cases, three different offsets were chosen in order to compare the effect of offset designs.

4. Results and discussion

In this section, the vortex dimensions and drag data will be presented for the continuous and segmented riblet configurations. This data will be used to compare the different configurations and show the differences between vortex dimensions and drag change for the different cases. The relationships between vortices and riblet geometry will also be presented.

4.1. Continuous riblets

In order to understand the effect of Reynolds number on lateral vortex dimensions of height and width, the Reynolds number was changed through modifying the velocity term as in Eq. 8 and the resulting vortex dimensions were measured on the flat surface. In **Fig. 6**, images of typical streamwise vortices on the flat surface for each case are presented. It should be noted that y^+ of interest in riblet modeling is less than about 30 referring to the viscous sublayer and buffer layer. The figure shows the streamwise vortices with the vortex centers located in the buffer layer increasing their lateral dimensions as the Reynolds number increases. The diameters increased from approximately 20 to 45 non-dimensional units from the smallest to largest Reynolds number of 2500 to 13,000.

Even though **Fig. 7** shows an image of typical streamwise vortices, their lateral dimensions varied within each case. **Figure 7a** shows a wider view of the flat surface at $Re = 4180$ showing more vortices with a wide variation in height and width. These vortices are generally all near the flat surface generating high drag as they produce burst and sweep motions. **Figures 7b,c** show a riblet surface with two different riblet spacings where **Fig. 7b** has $s^+ = 16$, $h^+ = 8$, $t^+ = 0.3$, $Re = 4180$ and **Fig. 7c** has $s^+ = 41$, $h^+ = 8$, $t^+ = 0.3$, $Re = 4180$. In **Fig. 7b**, the smaller spacing, $s^+ = 16$, shows vortices being lifted up above the surface, whereas in **Fig. 7c** with the larger spacing, $s^+ = 41$, shows vortices not being lifted away from the surface. With the larger spacing, the vortices are able to fit within the riblet gaps generating high drag. **Figure 7d** shows a zoomed in view of one section of **Fig. 7b**. Because the vortex generates transverse velocity above the riblets, vortices in the riblet valleys can be created. These riblet valley vortices do not generate as much drag as the streamwise vortices because they do not produce as strong of burst and sweep motions since they are located below the higher velocity fluid in the channel. Vortex structures and their strength can be viewed by plotting normalized Q criterion which is the second invariant of the velocity gradient tensor and represents the local balance between vorticity magnitude and strain rate. This criterion can help to visualize turbulence and view vortices.[47] The riblet valley vortices are not as strong as the streamwise

vortices as shown by the normalized Q criterion in **Fig. 7e**. The normalized Q criterion value for the riblet valley vortices is too small to view.

In **Fig. 7**, more velocity vector arrows protrude through the riblet surface wall than in the flat surface wall. This difference could be due to riblets creating riblet valley vortices (**Fig. 3**) which can create additional regions where the flow can be directed toward the wall. A flat surface will not have the flow run up against a projecting object to change the flow direction. The protruding arrows on the flat surface originate at locations where vortices interact.

In order to understand the effect of the parameters on drag change, each parameter was individually modified and the resulting drag change was calculated and shown in **Fig. 8** where the negative drag change values indicate a drag reduction. In **Fig. 8a**, the models with different s^+ were plotted. The varying velocity and viscosity was plotted separately than the varying spacing because when velocity or viscosity changes so does the Reynolds number. Furthermore, the h^+/s^+ was kept constant in the varying velocity and viscosity models whereas in the varying spacing models the height was kept constant at $h^+ \approx 8$ and so the h^+/s^+ ratio varied between the cases. The varying velocity and viscosity curve has a maximum drag reduction at $s^+ = 20$ at 10%. Because the varying velocity and viscosity data is similar, it shows that the riblet geometry does not depend on the dimensional parameters, but the non-dimensional parameters as given in Eq. 1 and 3–4. The non-dimensional parameters will give the same drag reduction regardless of which non-dimensional parameters are changed. The experimental data using blade riblets from Bechert et al.[5] was also plotted to show the similarities between the modeling and experimental work. The Reynolds number plotted on the top axis refers to the data set in Martin and Bhushan.[23]

The maximum drag reduction for the varying spacing models was 11% at $s^+ = 23$. This change in s^+ location is due to the riblet height staying constant whereas in the previous models the riblet height varied. The differences between these curves is more apparent at the larger s^+ values because the height difference is greater. When the height is too large, the riblet protrude too far into the flow generating higher drag. This result caused the varying velocity and viscosity trendline to curve upward faster than the varying spacing trendline. When the riblet height remains constant and the spacing changes (**Fig. 8a** right), many riblet peaks contact vortices leading to less of a drag reduction at small spacing. At large spacing, the vortices can fit within

the valleys and are not lifted up leading to a drag increase. From these plots, it is apparent that both riblet spacing and height play a significant role in determining drag change.

Furthermore, in **Fig. 8b** with only varying riblet height, there is a dramatic drag change between the different cases. One curve shows $s^+ = 16$ whereas the other curve shows $s^+ = 23$; however, in both cases the maximum drag reduction occurred when $h^+ = 8 - 10$ even with different Reynolds numbers and riblet spacings. Increasing outside of this range quickly led to a drag increasing state due to the riblets protruding too far into the higher velocity flow, and decreasing below this range led to a less efficient state due to the riblets unable to effectively repel the vortices.

When the riblet thickness was modified, little drag change occurred as shown in **Fig. 8c**. A roughly constant 9% drag reduction was found for thicknesses ranging from $t^+ = 0.08 - 0.50$. There were slight oscillations around this value, but because there was not a strong positive or negative relationship, the trend was reported as constant over this range. At much larger thicknesses, the width of the riblet valleys would decrease and the width of the riblet peaks would increase. It is expected that these changes would generate a weaker drag reduction, and eventually a drag increase.

With the wide variation in lateral vortex dimensions as shown in **Fig. 7a**, the dimensions of many vortices were measured using *y*-*z* planes with vorticity contours and tangential velocity vectors and averaged. In **Fig. 9**, the average vortex dimensions on the flat and riblet surfaces were plotted. **Fig. 9a** shows effect of Reynolds number as well as s^+ changed by changing velocity (left) and effect of spacing for a constant Reynolds number (right). For varying velocity, as the velocity was increased, the height and width of the vortices became larger on both surfaces suggesting that an increase in Reynolds number increases the lateral dimensions of the vortices. **Figures 9b** and **9c** show effect of *h* and *t*, respectively. In **Fig. 9a-c** for varying spacing, height, and thickness, the vortex lateral dimensions were fairly constant. These figures show that only when the Reynolds number increases does the lateral dimensions of the streamwise vortex change. In these figures, the smooth surface vortex width averaged 37 non-dimensional units; the riblet surface vortex width averaged 32 non-dimensional units; the smooth surface vortex height averaged 23 non-dimensional units; and the riblet surface vortex height averaged 19 non-dimensional units.

In all cases for both surfaces, the vortex width was larger than the vortex height and the flat surface had larger vortex dimensions than the riblet surface. Because the sides of the model used periodic conditions, the vortices could grow in the spanwise direction; however, the riblet and flat surfaces impeded the growth in the height direction. The vortex dimensions on the riblet surface were smaller than the flat surface because the riblets protruded sharply into the flow obstructing vortex rotation and growth.

The drag change and vortex size data were compared to determine when vortices were optimally lifted. The optimal drag reduction occurred at $s^+ = 18 - 20$ and $s^+ = 23$ from **Fig. 8a**. By comparing these s^+ values with the riblet surface vortex width on **Fig. 9a**, it was found that the average riblet surface vortex width was approximately 32 non-dimensional units. This corresponded to a vortex-width-to-spacing ratio of approximately 1.5. As the spacing and riblet surface vortex width approached the same value, drag became larger and eventually became a drag-increasing case. It is thought that this ratio is effective in lifting away the vortices from the surface and minimizing bursts and sweeps. As the size of the vortices and spacing approached the same value, there was a greater possibility of a vortex fitting within a riblet valley and increasing drag.

4.2. Segmented riblets

In order to compare continuous riblet results to segmented riblet results and better understand the riblet segmentation in sharks, various segmented riblet cases were modeled. The parameters for the length of each riblet (L_1), the gap between the riblets (L_2), and the offset between riblets (L_3) were modified independently. In **Fig. 10**, a model with $s^+ = 16$, $h^+ = 8$, $t^+ = 0.3$, $Re = 4180$, $L_1^+ = 68$, and $L_2^+ = 101$ shows how vortices interact with an aligned-segmented riblet surface. In **Fig. 10a**, a *y-z* plane was taken through the riblets and shows typical vortices near the flat surface and vortices of various sizes lifted on the riblet surface. In **Fig. 10b**, a *y-z* plane was taken through the gap between riblets. Again, typical vortices are shown near the flat surface. On the riblet surface, there are vortices that were lifted above the surface and others that sit below the riblet peaks. These vortices can be seen because the velocity vectors are shown going through the height of the riblet; however, because the plane does not have any riblets, it shows that the vortices are not being lifted. This figure shows that streamwise vortices can fit within the gaps between riblets with other vortices being lifted up above the riblets.

In order to better understand the role of riblet gap, **Fig. 11** shows a model with a larger gap size compared to the model in **Fig. 10** ($L_2^+ = 154$ compared to $L_2^+ = 101$ with the same $s^+ = 16$, $h^+ = 8$, $t^+ = 0.3$, and $Re = 4180$). This case has a similar riblet length ($L_1^+ = 66$ compared to $L_1^+ = 68$), but a greater gap between the riblets. **Figure 11a** shows the same vortex patterns as in **Figure 10a** on both the flat and riblet surfaces. The flat surface has the vortices near the wall whereas the riblet surface has vortices that are lifted away. In **Fig. 11b**, the riblet surface shows more vortices not being lifted away from the surface when compared to **Fig. 10b**. By comparing **Figs. 10** and **11**, it shows that increasing the gap between the riblets increases the chance that a vortex will not be lifted in the gaps between the riblet surface. On the other hand, on a plane through the riblets, the vortices will still be lifted away.

By plotting the normalized Q criterion for all the models, the lengths and diameters of the streamwise vortices can be seen and measured. **Figure 12a** shows the normalized Q criterion plotted for $s^+ = 16$, $h^+ = 8$, $t^+ = 0.3$, $Re = 4180$, $L_1^+ = 67$, and $L_2^+ = 17$ with a streamwise vortex pointed out on the flat and riblet surface as an example case. Using these images, the lengths and diameters of the streamwise vortices could be calculated to understand the relationship between streamwise vortices and drag. In **Figure 12b**, the distribution of the vortex diameters was plotted for the flat and riblet surfaces. The riblet surface has a greater likelihood of a smaller diameter than the flat surface because the riblets sharp edges deter vortex growth. The average vortex diameter is predominately between $d^+ = 20 - 50$. From **Fig. 8a** with optimal riblet spacing of $s^+ \approx 20$, the spacing would lift the majority of the vortices from the surface. **Figure 12c** shows the distribution of the streamwise vortex lengths on the flat and riblet surfaces. For the vortex length of 100–200 non-dimensional units, over 80% of the vortices on both surfaces are within this range. This result is consistent with the findings by Lyons et al.[38] and Garcia-Mayoral and Jimenez.[40]

The streamwise vortex length data helps to explain the trends found by plotting the drag change data for the models as shown in **Fig. 13**. In **Fig. 13a**, the aligned-segmented models were plotted for varying L_1^+ with constant L_2^+ and then also with constant L_1^+ with varying L_2^+. In the varying L_1^+ with constant L_2^+ data set, the drag change increases as the length of the riblets increase. As the lengths increase, fewer gaps on the riblet surface occur leading to more of a continuous case which showed a greater drag reduction. Fewer gaps lead to less chance of burst and ejection events in the gaps. In the constant L_1^+ with varying L_2^+ data set, the drag change

decreases to a drag reduction of 5.0% at $L_2^+ = 101$ and then increases after that. With streamwise vortices predominately having non-dimensional lengths in the 100–200 range, once the gap becomes larger than 100 non-dimensional units, the streamwise vortex is not lifted, generating a lot of drag. In **Fig. 13b**, the staggered-segmented data set is plotted showing a constant drag reduction of 3.3%. For the values of $L_1^+ = 67$ and $L_2^+ = 17$, varying L_3^+ did not affect the drag change.

Modeling shows that aligned-segmented and staggered-segmented riblets result in drag reduction of approximately 5% and 3%, respectively, lower than that in the continuous riblet configuration of approximately 10%. Thus it raises the question why do sharks have segmented and/or staggered riblets? It is believed that segmented riblets help the shark to swim by creating a deformable surface and/or in ejection of contaminant particles. Because each scale can individually pivot, when the shark turns, the surface of the shark becomes a deformable surface. Staggered riblets give particles a path to be removed from the surface. Aligned-segmented riblets may have less of a chance for particles to be ejected. Whereas, continuous riblets may have the least chance for contaminants to be removed from the riblet valleys. By discouraging contaminant settlement and eventual growth, the riblet valleys in segmented configurations stay unpolluted and the drag reduction stays effective.

5. Conclusions

Nature has produced geometrical structures on the scales of fast-swimming sharks that can reduce drag. The microscopic grooves found on these scales, known as riblets, have been shown to reduce drag compared to a flat surface on the order of 10%. These riblet structures need to have appropriately sized dimensions in order to lift streamwise vortices to minimize transverse shear stresses. Previously, continuous and segmented riblet configurations have been studied; however, no modeling has been completed for segmented configurations. Segmented configurations are commonly seen on the scales of sharks, and therefore, the reasons behind nature's design should be understood. Furthermore, the relationship between vortex dimensions and riblet geometry needed to be explored both for continuous and segmented configurations. By understanding the continuous and segmented configurations and the relationship between vortex dimensions and riblet geometry the drag reduction mechanism can be better understand and better drag reduction surfaces can be created.

In this research, gaps and offsets in a blade riblet geometry were independently changed to create various aligned-segmented and staggered-segmented, riblet configurations. The drag and vortex formations were analyzed and compared to a flat surface and other continuous riblet configurations. On a flat surface, streamwise vortices were observed in the buffer layer with average diameters ranging from 20 to 45 non-dimensional units depending on Reynolds number. These vortices had lengths that were predominately in the 100–200 non-dimensional unit range.

In the continuous configurations, it was found that when the vortices were approximately 1.5 times as large as the riblet spacing, optimal drag reduction was seen. Drag reductions of approximately 10% occurred when $s^+ \approx 18 - 25$ and $h^+ \approx 8 - 10$ which was similar to $s^+ = 16$ and $h^+ = 8$ from Bechert et al.[5] and $s^+ = 18$ and $h^+ = 9$ from El-Samni et al.[24] With these riblet dimensions, the streamwise vortices were lifted from the surface reducing the drag on the surface. These lifted vortices created riblet valley vortices due to the transverse velocity from the streamwise vortex, but the riblet valley vortices do not significantly affect drag due to their decreased strength and decreased ability in generating burst and sweep motions. To show that the non-dimensionalizing method was valid, the velocity and viscosity terms were independently changed and then the drag change was shown to have the same trend.

The aligned-segmented and staggered-segmented riblet configurations had maximum drag reductions of approximately 5% and 3%, respectively. The three parameters of riblet length, gap length, and riblet offset each changed the reported drag differently. When the lengths of the riblets increased with constant gap size, the drag reduction increased due to the configuration more closely approximating the continuous configuration. As the gap length approached 100 non-dimensional units, the drag reduction increased with the drag increasing after due to the increased odds of streamwise vortices falling into the gaps between consecutive riblets. As the riblet offset increased, no differences in drag change were observed.

Continuous configurations have a drag reduction of approximately 10% which is greater than aligned-segmented and staggered-segmented at approximately 5% and 3%, respectively. With the decreased drag reduction in staggered and segmented configurations, the question of why do sharks implement these designs is raised. First, it may help create a deformable surface by allowing the scales to pivot, helping the shark to swim. Second, it may help in contaminant removal by giving particles a path to be removed from the surface.

The conclusions drawn from studying drag and vortex interactions on a flat surface and continuous and segmented riblet surfaces are presented in **Fig. 14**. **Figure 14a** shows a typical streamwise vortex near a flat surface, and in **Fig. 14b** with $s^+ = 25.3$ or $s^+ = 41.2$, $h^+ = 8$, $t^+ = 0.3$, and $Re = 4180$, the vortex can be lifted or not lifted depending on the riblet spacing. As the spacing decreases below the optimum, drag reduction becomes less optimal due to vortices interacting with many riblet peaks. As the spacing increases above the optimum, drag increases due to vortices not being lifted. An example drag reduction curve for varying riblet spacing is shown in **Fig. 14c**. **Figure 14d** with $s^+ = 16$, $h^+ = 8$, $t^+ = 0.3$, $Re = 4180$, $L_1^+ = 66$, and $L_2^+ = 66$ or $L_2^+ = 154$ shows that choosing a gap size smaller than the length of the streamwise vortex allows for the vortices to be lifted from the surface reducing drag in a segmented configuration.

Table 3 summarizes the effect of the continuous and segmented riblet parameters. The riblet spacing should be around 15–20 non-dimensional units to lift the vortices with the riblet height around 8–10 non-dimensional units. If the riblets are too tall, they protrude too far into the flow and increase drag. If they are too short, they do not effectively lift the vortices, which in both cases, increases drag. Thinner riblets are better because the majority of the drag is found at the riblet peaks; however, thin riblets below a certain value do not noticeably change the drag. Riblet gaps should be less than 100 non-dimensional units to repel the streamwise vortices that predominately are 100–200 non-dimensional units long. Riblet offsets do not noticeably affect drag when independently modified. Because continuous riblets have a greater drag reduction than aligned-segmented and staggered-segmented riblets, sharks may implement segmentation for two reasons. These configurations may help create a deformable surface for shark movement and/or in ejection of contaminant particles to keep the shark skin surface clean.

Understanding different riblet configurations helps lead to a better understanding of the riblet mechanism which can be used as drag-reduction design principles for industrial applications in marine, medical, and industrial fields. Riblet dimensions are dependent on the component size and can range from the micro- to nanoscale.

6. Acknowledgements

The authors would like to thank Professor T. Conlisk for his insightful discussion regarding vortices. This work was supported in part by an allocation of computing time from the Ohio Supercomputer Center.

References

1 B. Bhushan, "Biomimetics: lessons from nature – an overview", *Phil. Trans. R. Soc.,* 2009, **367**, 1445-1486.

2 B. Bhushan, *Biomimetics: Bioinspired Hierarchical-Structured Surfaces for Green Science and Technology*, Springer-Verlag, Heidelberg, Germany, 2012.

3 W. Reif, *Squamation and Ecology of Sharks.* Courier Forschungsinstitut Senckenberg, Frankfurt, Germany, 1985, **78**, 1–255.

4 D. M. Bushnell and K. J. Moore, "Drag reduction in nature", *Annu. Rev. Fluid Mech.,* 1991, **23**, 65–79.

5 D. W. Bechert, M. Bruse, W. Hage, J. G. T. van der Hoeven and G. Hoppe, "Experiments on drag reducing surfaces and their optimization with an adjustable geometry", *J. Fluid Mech.,* 1997, **338**, 59–87.

6 B. Dean and B. Bhushan, "Shark-skin surfaces for fluid-drag reduction in turbulent flow: a review", *Phil. Trans. R. Soc.,* 2010, **368**, 4775–4806.

7 G. D. Bixler and B. Bhushan, "Fluid drag reduction with shark-skin riblet inspired microstructured surfaces", *Adv. Funct. Mater.,* 2013, **23**, 4507–4528.

8 Y.C. Jung and B. Bhushan, "Biomimetic structures for fluid drag reduction in laminar and turbulent flows", *J. Phys.: Condens. Matter,* 2010, **22**, 035104.

9 G. D. Bixler and B. Bhushan, "Bioinspired rice leaf and butterfly wing surface structures combining shark skin and lotus effects", *Soft Matt.,* 2012, **8**, 11271-11284.

10 B. Bhushan, *Springer Handbook of Nanotechnology*, 3rd ed., Springer, New York, 2010.

11 M. J. Walsh and J. B. Anders, "Riblet/LEBU research at NASA Langley", *Appl. Sci. Res.,* 1989, **46**, 255–262.

12 K. Krieger, "Do pool sharks really swim faster?" *Science,* 2004, **305**, 636–637.

13 G. D. Bixler, A. Theiss, B. Bhushan and S. C. Lee, "Anti-fouling properties of microstructured surfaces bio-inspired by rice leaves and butterfly wings", *J. Colloid Interf. Sci.,* 2014, **419**, 114-133.

14 M. J. Walsh, "Turbulent boundary layer drag reduction using riblets", Paper #AIAA-1982-0169, presented at *AIAA 20th Aerospace Sciences Meeting*, Orlando, FL, 1982.

15 J. J. Rohr, G. W. Andersen, L. W. Reidy and E. W. Hendricks, "A comparison of the drag-reducing benefits of riblets in internal and external flows", *Exp. Fluids,* 1992, **13**, 361–368.

16 D. W. Bechert, M. Bruse and W. Hage, "Experiments with three-dimensional riblets as an idealized model of shark skin", *Exp. Fluids*, 2000, **28**, 403–412.

17 G. D. Bixler and B. Bhushan, "Shark skin inspired low-drag microstructured surfaces in closed channel flow", *J. Colloid Interface Sci.,* 2013, **393**, 384–396.

18 D. C. Chu and G. E. Karniadakis, "A direct numerical simulation of laminar and turbulent flow over riblet-mounted surfaces", *J. Fluid Mech.,* 1993, **250**, 1–42.

19 H. Choi, P. Moin and J. Kim, "Direct numerical simulation of turbulent flow over riblets", *J. Fluid Mech.,* 1993, **255**, 503–539.

20 D. Goldstein, R. Handler and L. Sirovich, "Direct numerical simulation of turbulent flow over a modelled riblet-covered surface", *J. Fluid Mech.,* 1995, **302**, 333–376.

21 S. J. Lee and S. H. Lee, "Flow field analysis of a turbulent boundary layer over a riblet surface", *Exp. Fluids,* 2001, **30**, 153–166.

22 A. Mohammadi and J. Floryan, "Groove optimization for drag reduction", *Phys. Fluids*, 2013, **25**, 113601.

23 S. Martin and B. Bhushan, "Fluid flow analysis of a shark-inspired microstructure", *J. Fluid Mech*., 2014, **756**, 5–29.

24 O. A. El-Samni, H. H. Chun and H. S. Yoon, "Drag reduction of turbulent flow over thin rectangular riblets", *Int. J. Eng. Sci.,* 2007, **45**, 436-454.

25 B. R. Munson, T. H. Okiishi, W. W. Huebsch and A. P. Rothmayer, *Fundamentals of Fluid Mechanics*, 7th edn., Wiley, Hoboken, NJ, 2012.

26 P. S. Klebanoff, "Characteristics of turbulence in a boundary layer with zero pressure gradient", *NACA TN-3178*, 1954.

27 S. J. Kline, W. C. Reynolds, F. A. Schraub and P. W. Runstadler, "The structure of turbulent boundary layers", *J. Fluid Mech*., 1967, **30**, 741–773.

28 S. K. Robinson, "Coherent motions in the turbulent boundary layer", *Ann. Rev. Fluid Mech*., 1991, **23**, 601–639.

29 D. B. Spalding, "A single formula for the law of the wall", *Trans. ASME J. Appl. Mech.,* 1961, **28**, 455–458.

30 F. White, *Viscous Fluid Flow,* 3rd ed., McGraw Hill, New York, 2006.

31 T. L. Hon and J. D. Walker, "An analysis of the motion and effects of hairpin vortices", *Interim Report, Lehigh Univ., Bethlehem, PA. Dept. of Mechanical Engineering and Mechanics*., 1987, 1.

32 S. K. Robinson, "A review of vortex structures and associated coherent motions in turbulent boundary layers", in *Structure of Turbulence and Drag Reduction*, pp. 23–50, Springer, 1990.

33 R. W. Johnson, *Handbook of Fluid Dynamics*, CRC, Boca Raton, FL, 1998.

34 H. Kim, S. J. Kline and W. C. Reynolds, "The production of turbulence near a smooth wall in a turbulent boundary layer", *J. Fluid Mech.,* 1971, **50**, 133–160.

35 R. F. Blackwelder and H. Eckelmann, "Streamwise vortices associated with the bursting phenomenon", *J. Fluid Mech.,* 1979, **94**, 577–594.

36 J. D. Swearingen and R. F. Blackwelder, "The growth and breakdown of streamwise vortices in the presence of a wall", *J. Fluid Mech.,* 1987, **182**, 255–290.

37 J. Kim, P. Moin and R. Moser, "Turbulence statistics in fully developed channel flow at low Reynolds number", *J. Fluid Mech.,* 1987, **177**, 133–166.

38 S. L. Lyons, T. J. Hanratty and J. B. McLaughlin, "Turbulence-producing eddies in the viscous wall region", *AIChE journal,* 1989, **35**, 1962–1974.

39 T. L. Doligalski, C. R. Smith and J. D. A. Walker, "Vortex interactions with walls", *Ann. Rev. Fluid Mech.,* 1994, **26**, 573–616.

40 R. Garcia-Mayoral and J. Jimenez, "Hydrodynamic stability and breakdown of the viscous regime over riblets", *J. Fluid Mech*., 2011, **678**, 317–347.

41 P. G. Saffman and G. R. Baker, "Vortex interactions", *Ann. Rev. Fluid Mech.,* 1979, **11**, 95–121.

42 J. C. Lasheras, J. S. Cho and T. Maxworthy, "On the origin and evolution of streamwise vortical structures in a plane, free shear layer*", J. Fluid Mech*., 1986, **172**, 231–258.

43 Ohio Supercomputer Center. "Glenn supercomputer", http://osc.edu/ark:/19495/hpc1ph70, 2009.

44 Anonymous, ANSYS® Fluent, Release 14.5, Help System, Fluent User's Guide, ANSYS, Inc., 2015.

45 D. C. Wilcox, *Turbulence modeling for CFD*. 3rd ed., DCW industries, La Canada, CA, 2006.

46 J. Jimenez and P. Moin, "The minimal flow unit in near-wall turbulence", *J. Fluid Mech.,* 1991, **225**, 213–240.

47 J. C. Vassilicos and J. Hunt, *Turbulence Structure and Vortex Dynamics*, Cambridge University Press, Cambridge, UK. 2000.

Table 1 Test cases for the simulations of turbulent flow over continuous riblets

	s (mm)	h (mm)	t (μm)	ν/V_l (μm)		s^+	h^+	t^+	Number of riblets
				Varying V_l $\nu = 10^{-6}$ m^{2}s^{-1}	Varying ν $V_l = 0.42$ ms^{-1}				
Baseline	**1.00**	**0.50**	**20.0**	**2.38**	**2.38**	**16.2**	**8.1**	**0.32**	**20**
Effect of V				4.00 **2.38** 1.39 0.98 0.76		10.3 **16.2** 24.5 32.4 46.8	5.1 **8.1** 12.3 16.2 23.4	0.21 **0.32** 0.49 0.65 0.94	20 **20** 20 20 20
Effect of ν					4.00 **2.38** 1.39 0.77	10.7 **16.2** 27.4 46.7	5.4 **8.1** 13.7 23.3	0.21 **0.32** 0.55 0.93	20 **20** 20 20
Effect of s	0.50 **1.00** 1.50 2.50					8.4 **16.2** 25.3 41.1	8.4 **8.1** 8.4 8.2	0.34 **0.32** 0.34 0.33	40 **20** 13 8
Effect of h		0.25 **0.50** 0.75				16.2 **16.2** 16.6	4.1 **8.1** 12.5	0.32 **0.32** 0.33	20 **20** 20
	0.75 0.75 0.75	0.22 0.32 0.42	15.0 15.0 15.0	1.20 1.20 1.20		22.9 23.2 23.2	6.7 9.9 13.0	0.46 0.46 0.46	27 27 27
Effect of t			5.0 10.0 **20.0** 30.0			16.8 17.0 **16.2** 16.6	8.4 8.5 **8.1** 8.3	0.08 0.17 **0.32** 0.50	20 20 **20** 20

Table 2 Test cases for the simulations of turbulent flow over segmented riblets

Riblet geometry	s = 1.0 mm, h = 0.5 mm, t = 20 μm, ν/V_j = 2.4 μm for Re = 4180 $s^+ \approx 16$, $h^+ \approx 8$, $t^+ \approx 0.3$						
	L_1 (mm)	L_2 (mm)	L_3 (mm)	L_1^+	L_2^+	L_3^+	Drag change
Continuous blade (L = 0.035 m)	∞	0	0	∞	0	0	- 9%
Aligned-segmented blade	2.0	1.0	0	32	16	0	- 2.1%
	4.0			67	17		- 3.3%
	6.0			99	17		- 4.3%
	4.0	1.0	0	67	17	0	- 3.3%
		2.0		68	34		- 3.6%
		4.0		66	66		- 3.7%
		6.0		68	101		- 5.0%
		9.4		66	154		+ 5.2%
Staggered-segmented blade	4.0	1.0	0.0	67	17	0	- 3.3%
			1.0	67	17	17	- 3.2%
			2.0	66	17	33	- 3.2%

Table 3 Summary of effect of riblet geometry on drag

Notes: Vortex non-dimensional diameters increase with *Re* – 20 to 45 for *Re* from 2500 to 13,000. Vortex non-dimensional lengths predominately range from 100 to 200.

(a) Continuous riblet conclusions

Parameter	Observation	Basis
Spacing (s^+)	Optimal riblet spacing should be around 15–20 non-dimensional units.	Vortices have a diameter of 30–40 non-dimensional units. With optimal riblet spacing, these vortices can be lifted up away from the riblet surface decreasing overall drag.
Height (h^+)	Optimal riblet height should be around 8–10 non-dimensional units.	Riblets that are too tall protrude too far into the flow increasing drag over the entire surface. Riblets that are too short do not effectively lift the vortices away from the surface decreasing sweeps and ejections.
Thickness (t^+)	Thinner riblets are better; however, at very small thicknesses, little drag differences are seen.	The majority of drag occurs at the riblet peaks and with thinner riblets, there is less drag at the peaks. Most of riblet surface area comes from the spacing and height parameters, and so, thickness plays a smaller overall role in drag change.

(b) Segmented riblet conclusions

Parameter	Observation	Basis
Riblet gaps	Riblet gaps should be smaller than streamwise vortex lengths to increase chances of lifting vortices. Gaps should have lengths less than 100 non-dimensional units.	Streamwise vortices predominately have lengths of 100–200 non-dimensional units and as gap length increases, the likelihood of a vortex fitting within the gap increases along with increasing drag.
Riblet offsets	Riblet offsets by themselves have little effect on drag, but increase the chance for contaminant particles to be ejected from the channels.	Riblets with offsets are still able to lift vortices from the surface decreasing sweep and ejection events associated with high drag.

(c) Continuous vs segmented configurations

Observation	Why segmented?
Continuous riblets have a drag reduction on the order of 10% whereas aligned-segmented and staggered-segmented have drag reductions on the order of 5% and 3%, respectively.	Segmented riblets may help sharks to swim by creating a deformable surface since the scales can individually pivot and/or in contaminant ejection to keep the shark clean by providing a path for particles to be removed

Figure Captions

Figure 1 Scanning electron microscopy (SEM) micrographs of shark skin samples shown at two magnifications. Actual Mako[9] (top) and replica Spiny Dogfish[8] (bottom). This Mako shark has riblets that have little gaps and no offsets (referred to as aligned-segmented riblets), whereas this Spiny Dogfish has gaps and offsets between the riblets (referred to as staggered-segmented riblets).

Figure 2 Turbulent flow visualization of streamwise vortices in a vertical cross-section over flat plate and riblet surfaces using atomized olive oil in air[21] showing how vortices were lifted up above a surface with appropriate riblet dimensions in order to obtain a drag reduction.

Figure 3 Model of vortex pair interaction on flat surface and single vortex interaction on riblet surface. A streamwise vortex has a diameter d^+ that ranges from 5–115 non-dimensional units[28] with an average diameter of 30 non-dimensional units[28,34,35,37] for the streamwise vortices with the center of the vortex in the buffer layer $5 \leq y^+ \leq 30$. Due to the streamwise vortices lifted above the riblets, vortices within the riblet valleys are formed. The longitudinal length of the streamwise vortex generally ranges from 100–200 non-dimensional units.[38,40]

Figure 4 (a) Computational domain of the riblet model for an aligned-segmented case showing geometry and riblet dimensions. The flat surface is on the top wall, and the riblet surface is on the bottom wall. (b) Configurations for the riblet geometry cases showing continuous; aligned-segmented; and staggered-segmented styles with the various riblet gap and offset parameters. (c) Vortex schematic showing lateral dimensions that were measured and analyzed.

Figure 5 Non-dimensional mean streamwise velocity profile over a flat surface in order to validate the simulation. The dashed lines refer to the linear law and the log-law with the log-law formulation of $V/v_\tau = 2.5 \ln y^+ + 5.5$. The dotted line refers to Spalding's law of the wall, and the solid line refers to the present study.

Figure 6 Streamwise vortices for Reynolds numbers ranging from 2500–13,000 showing vortex lateral dimensions with the diameter increasing as Reynolds number. The diameters increased from approximately 20 to 45 non-dimensional units.

Figure 7 Vortices on a flat surface compared to a riblet surface. (a) On a flat surface where $Re = 4180$, vortices are near the surface, (b) ($s^+ = 16$, $h^+ = 8$, $t^+ = 0.3$, $Re = 4180$) whereas on a riblet surface with a riblet spacing smaller than the vortex diameter, vortices are lifted up. (c) ($s^+ = 41$, $h^+ = 8$, $t^+ = 0.3$, $Re = 4180$) When the riblet spacing is larger than the vortex lateral dimensions, the vortices are not lifted from the surface, and fit within the riblet valleys increasing drag. (d) Due to transverse velocity from the vortices, there may be vortices within the riblet valleys. (e) The vortices above the riblets have a greater effect on drag due to the stronger rotation.

Figure 8 Drag change for the various models plotted against their non-dimensionalized parameter. (a) In the models with varying spacing, the varying velocity and viscosity curve shows an optimal drag reduction at $s^+ \approx 20$. (b) From the models with varying height, optimal

height was found to be at $h^+ \approx 8-10$. (c) The s^+ and h^+ terms affect drag significantly, whereas this range of t^+ did not affect drag notably.

Figure 9 Vortex lateral dimensions of height and width on the riblet and flat surfaces for the various models. With increasing velocity (a), Reynolds number based on channel height increases and vortex lateral dimensions also increases. In the models with varying *s*, *h*, or *t* (b-d), vortex lateral dimensions remains approximately constant. Average vortices have a greater width than height, and vortices on the flat surface are larger than on the riblet surface. Riblets pin the vortex keeping them from growing and becoming the same size as the vortices on the flat surface.

Figure 10 Vortices are shown on a flat and riblet surface with $s^+ = 16$, $h^+ = 8$, $t^+ = 0.3$, $Re = 4180$, $L_1^+ = 68$, and $L_2^+ = 101$. (a) Above the riblets, the vortices are lifted from the riblet surface. (b) In the gaps between the riblets, vortices can fall within the gaps or be lifted. On both planes, vortices on the flat surface are close to the flat surface.

Figure 11 Vortices are shown on a flat and riblet surface with $s^+ = 16$, $h^+ = 8$, $t^+ = 0.3$, $Re = 4180$, $L_1^+ = 66$, and $L_2^+ = 154$. When the gap between riblets becomes large enough, the streamwise vortices can fit within the gaps between riblets. (a) The vortices are shown lifted above the riblets. (b) The vortices are seen to have fallen below the riblets. The centers of the vortices are closer to the wall similar to the flat surfaces.

Figure 12 (a) Normalized Q criterion plotted on the computational domain to show streamwise vortices on the flat and riblet surfaces with $s^+ = 16$, $h^+ = 8$, $t^+ = 0.3$, $Re = 4180$, $L_1^+ = 67$, and $L_2^+ = 17$. The lengths and diameters of the streamwise vortices were measured to determine their distribution. (b) Distribution of the average diameter of streamwise vortices on flat and riblet surfaces. The average vortex diameter is between $d^+ = 20-50$. The flat surface has larger vortex diameters than the riblet surface because the riblets stop the vortices from becoming as large as they could become. (c) Distribution of the average length of streamwise vortices on flat and riblet surfaces. For the vortex length of 100–200 non-dimensional units, over 80% of the vortices on both surfaces are within this range.

Figure 13 (a) Drag change for the aligned-segmented cases. As L_1^+ increases, the riblet geometry approaches the continuous case and the drag reduction increases. As L_2^+ increases, the riblet geometry has greater gaps between the riblets, but the surface is still able to lift the streamwise vortices. The drag reduction stays constant and then increases to a drag increasing case once the gaps become on the order of the length of the streamwise vortex. (b) Drag change for the staggered-segmented cases. As L_3^+ increases, no difference in drag change is seen. It is thought that staggered-segmented riblets occur to help create a deformable surface for shark movement and in ejection of contaminant particles in the riblet valleys.

Figure 14 (a) On a flat surface, vortices are near the surface and generate a lot of drag. (b) ($s^+ = 25.3$ or $s^+ = 41.2$, $h^+ = 8$, $t^+ = 0.3$, and $Re = 4180$) With adequate riblet spacing size, streamwise vortices are lifted away from the surface reducing drag and creating an overall drag reduction surface. (c) Optimal drag reduction occurred when riblet spacing was approximately

23. (d) ($s^+ = 16$, $h^+ = 8$, $t^+ = 0.3$, $Re = 4180$, $L_1^+ = 66$, and $L_2^+ = 66$ or $L_2^+ = 154$) Gaps between the riblets can be created as long as the gaps remain shorter than the common streamwise vortex lengths of 100–200 non-dimensional units.

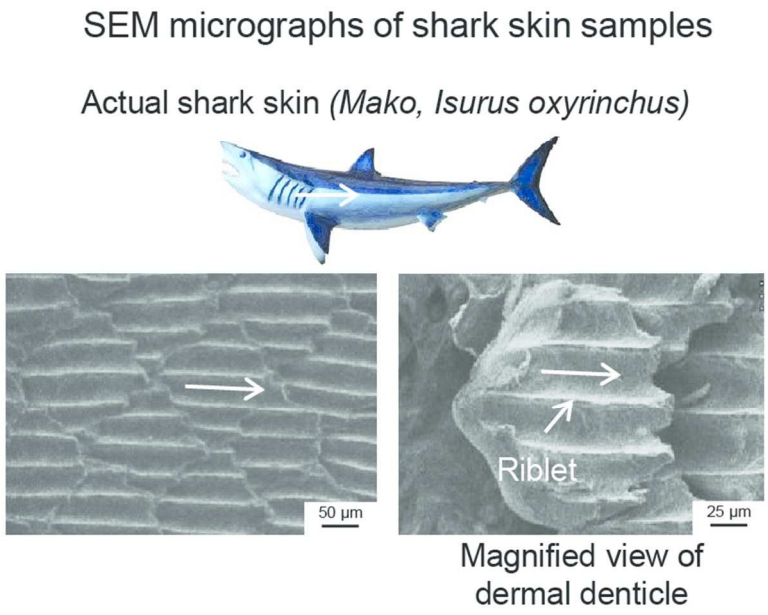

70x108mm (300 x 300 DPI)

Turbulent flow visualization of streamwise vortices by atomized olive oil smoke over a flat and riblet surface

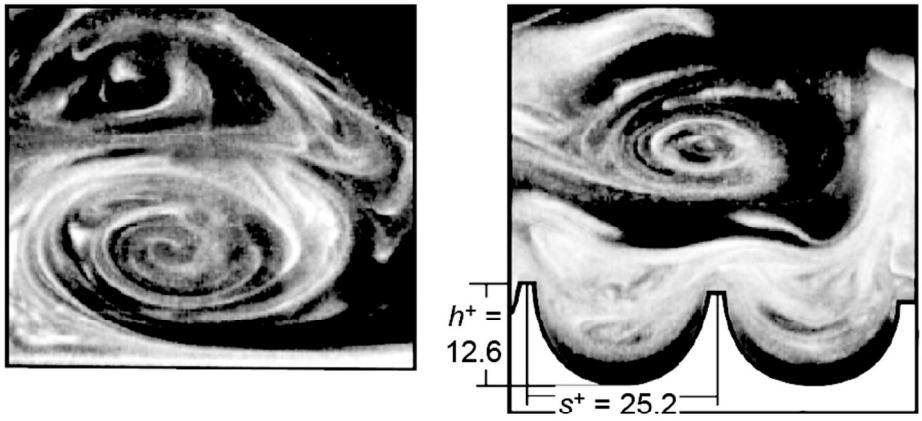

Flat surface Riblet surface

82x53mm (300 x 300 DPI)

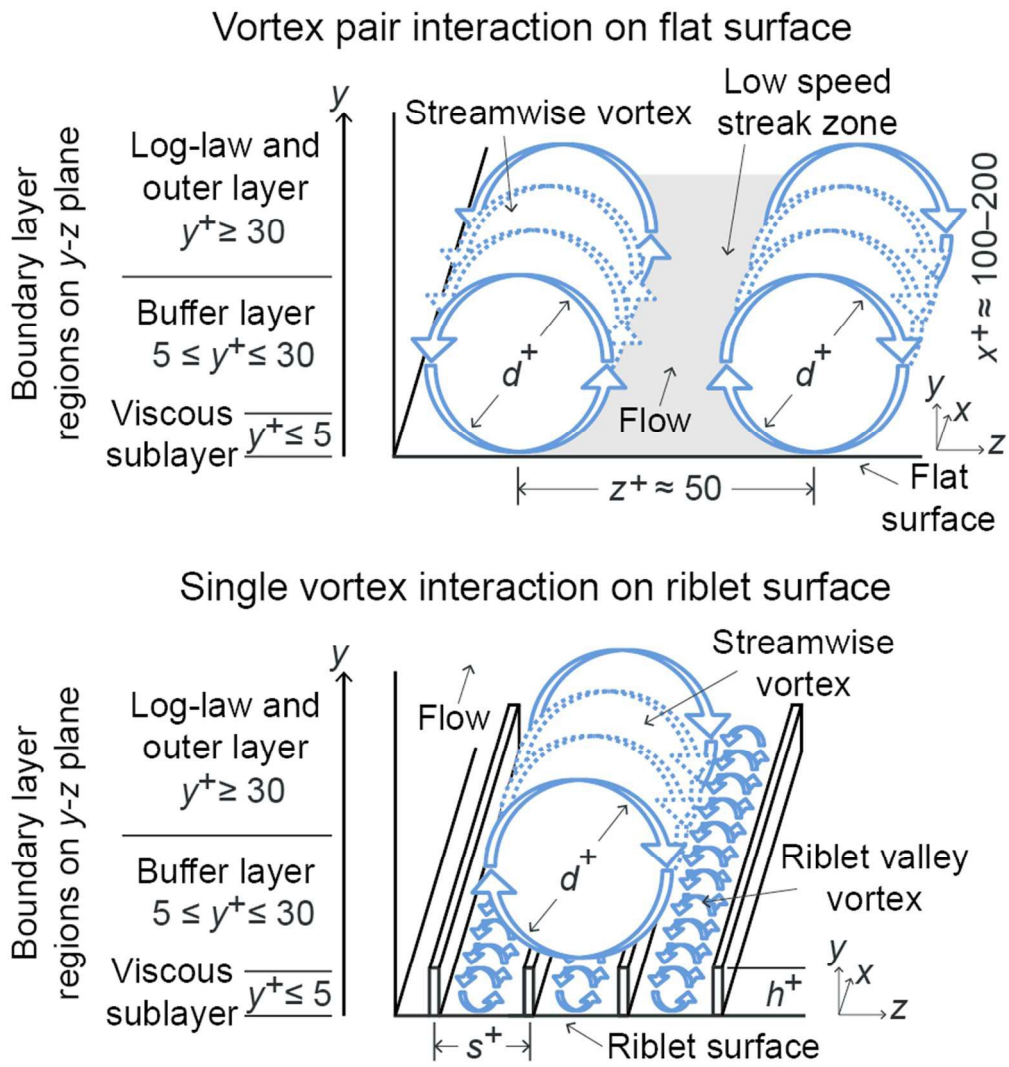

80x85mm (300 x 300 DPI)

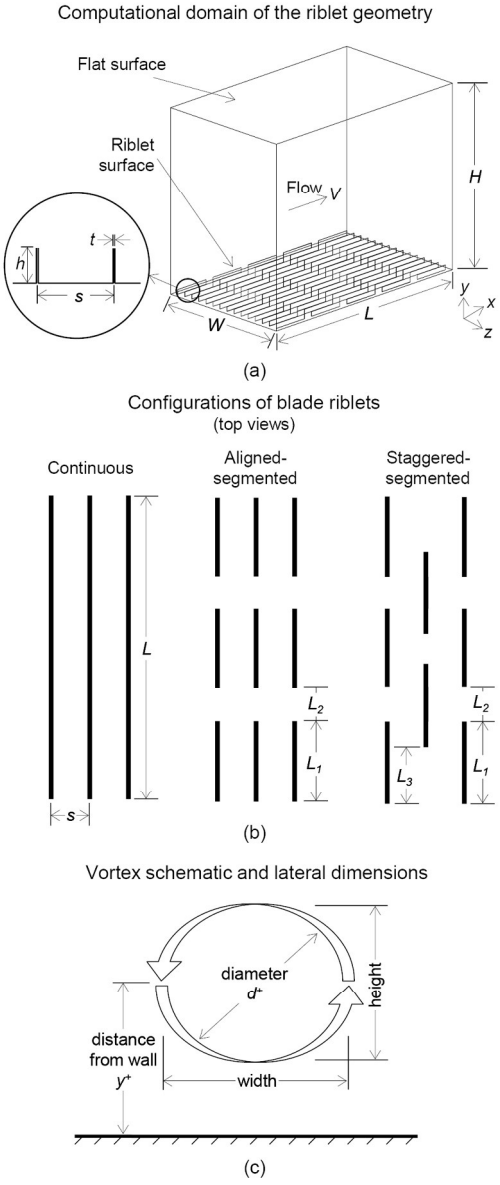

85x199mm (300 x 300 DPI)

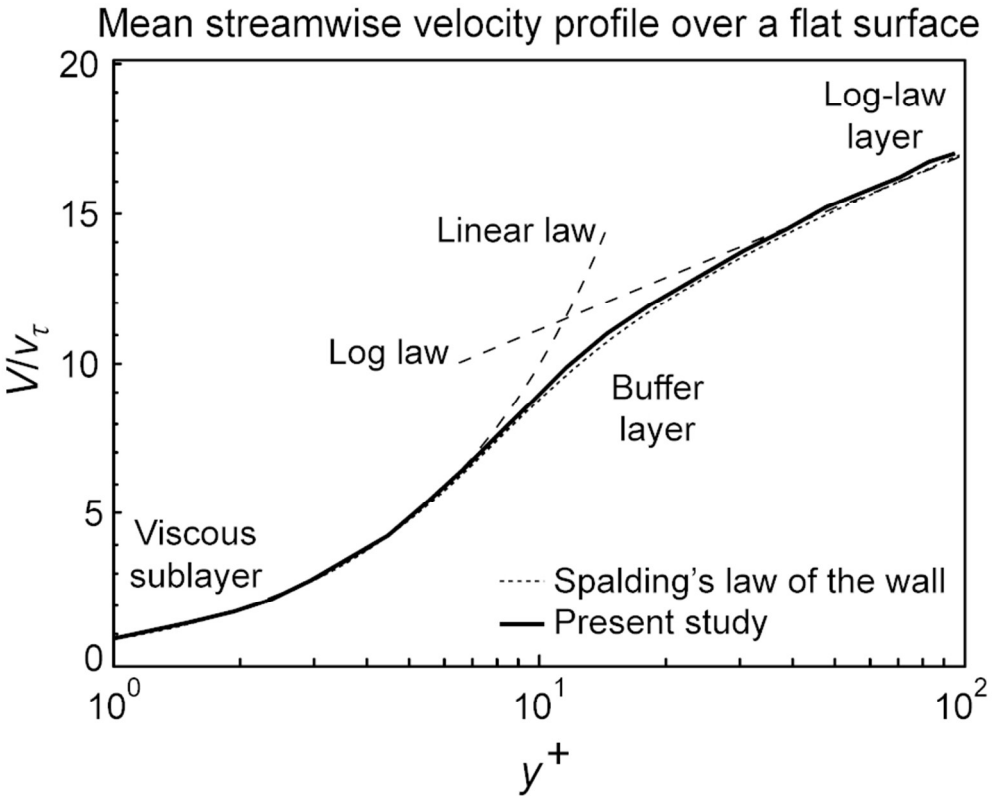

80x64mm (300 x 300 DPI)

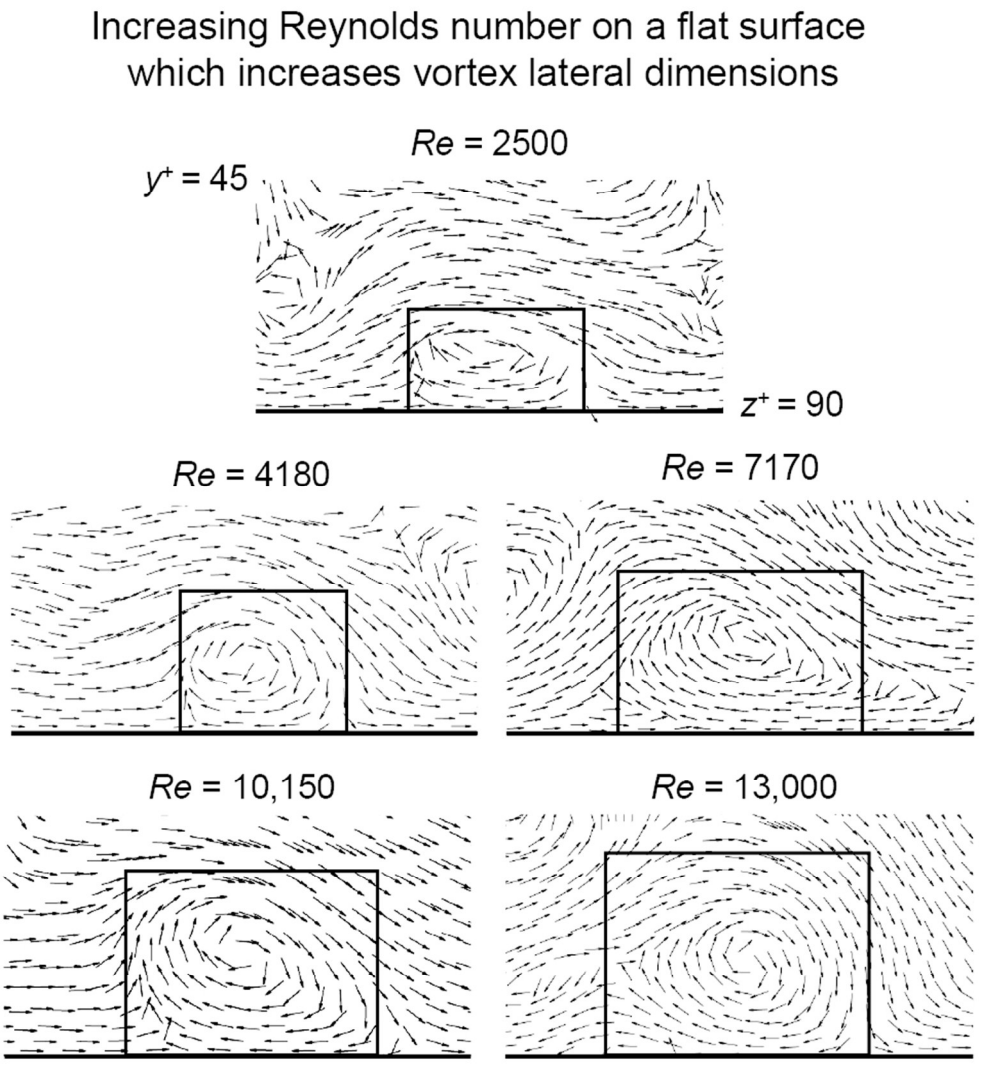

82x88mm (300 x 300 DPI)

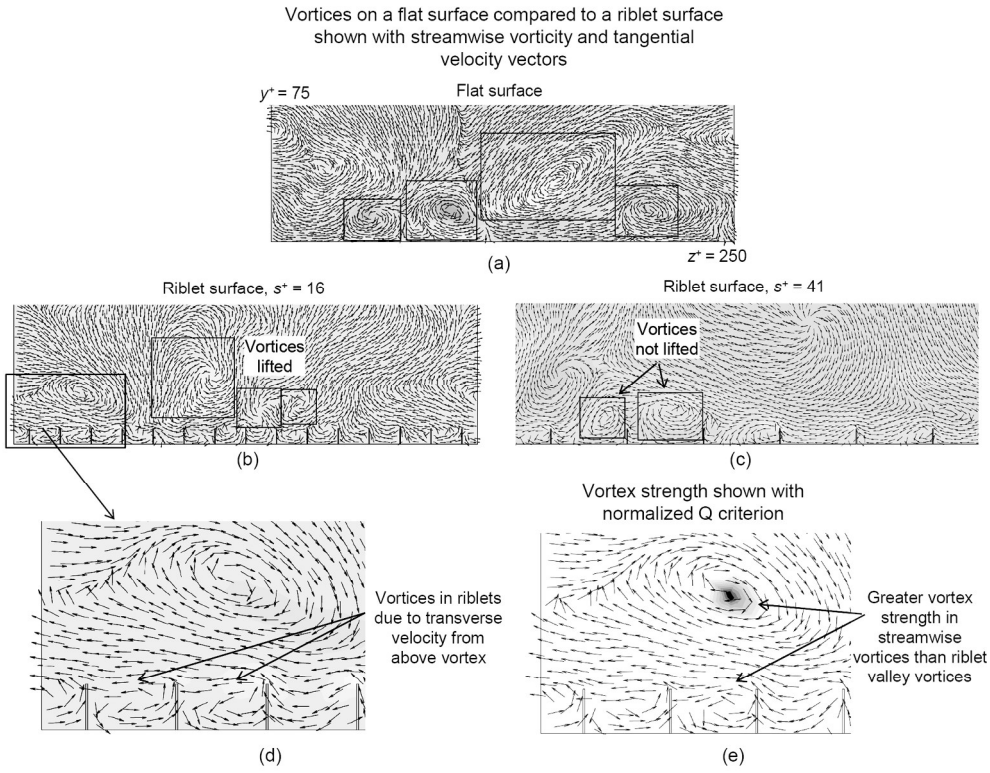

171x133mm (300 x 300 DPI)

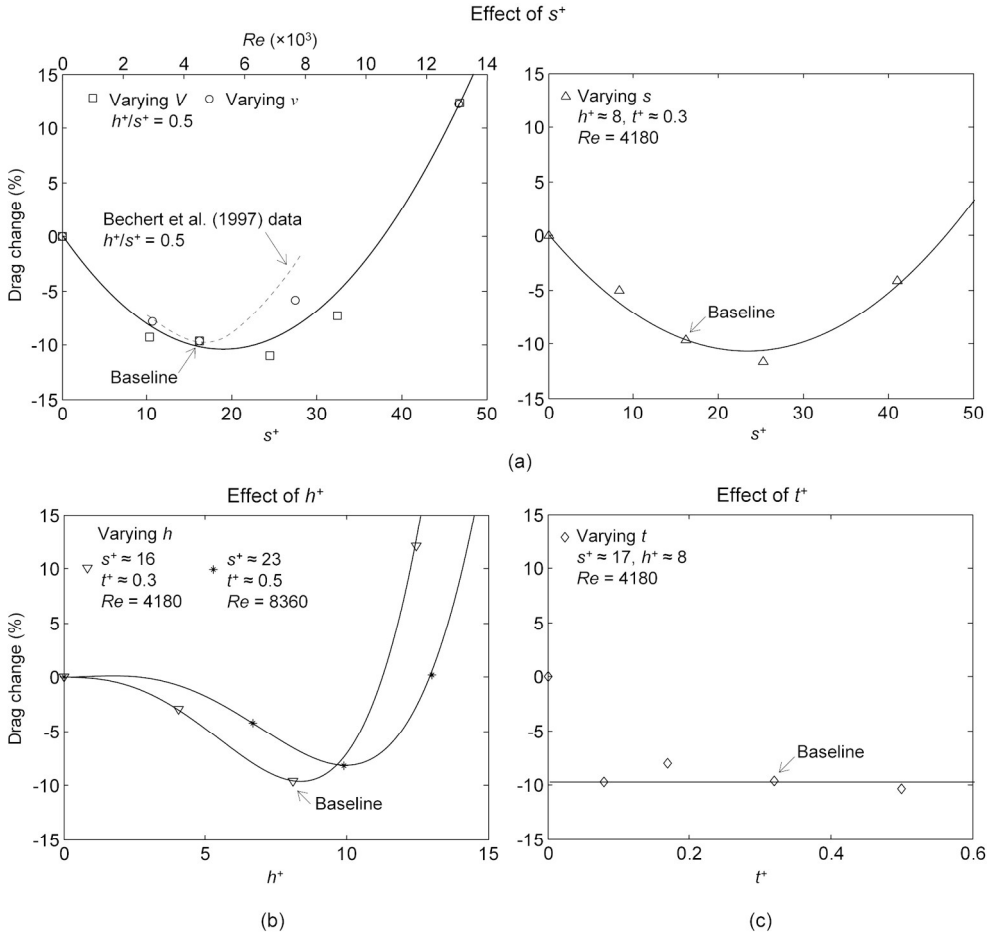

161x152mm (300 x 300 DPI)

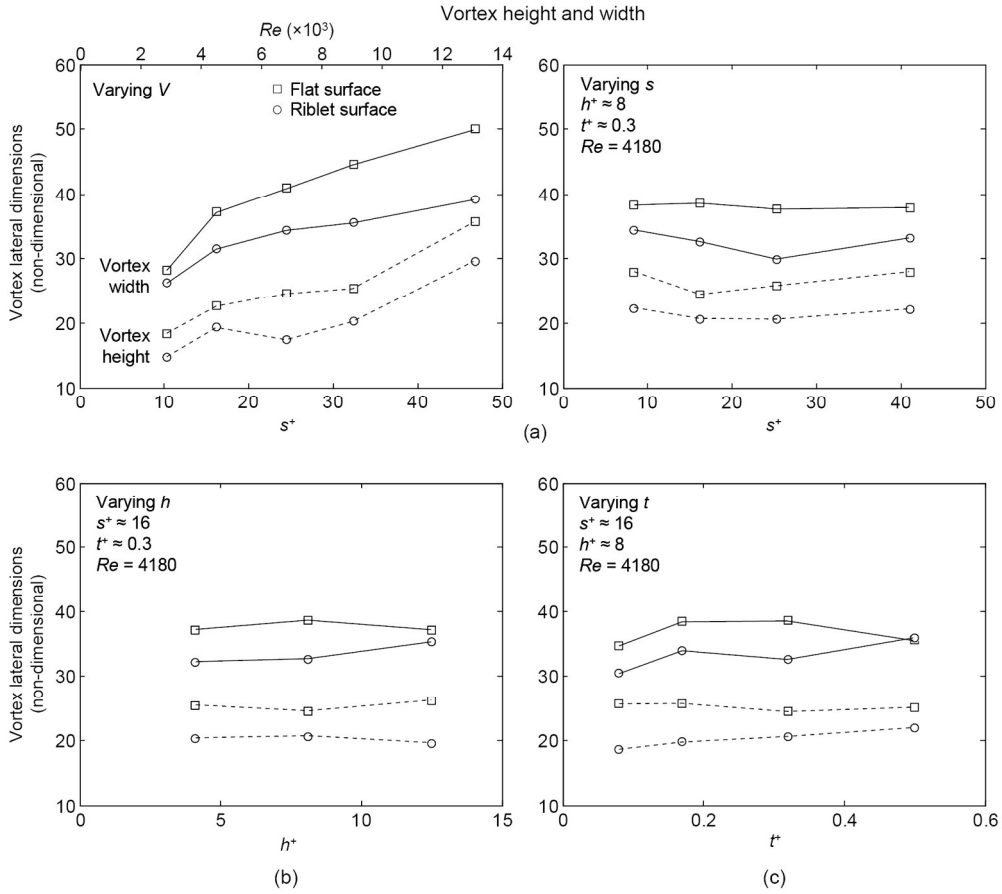

162x146mm (300 x 300 DPI)

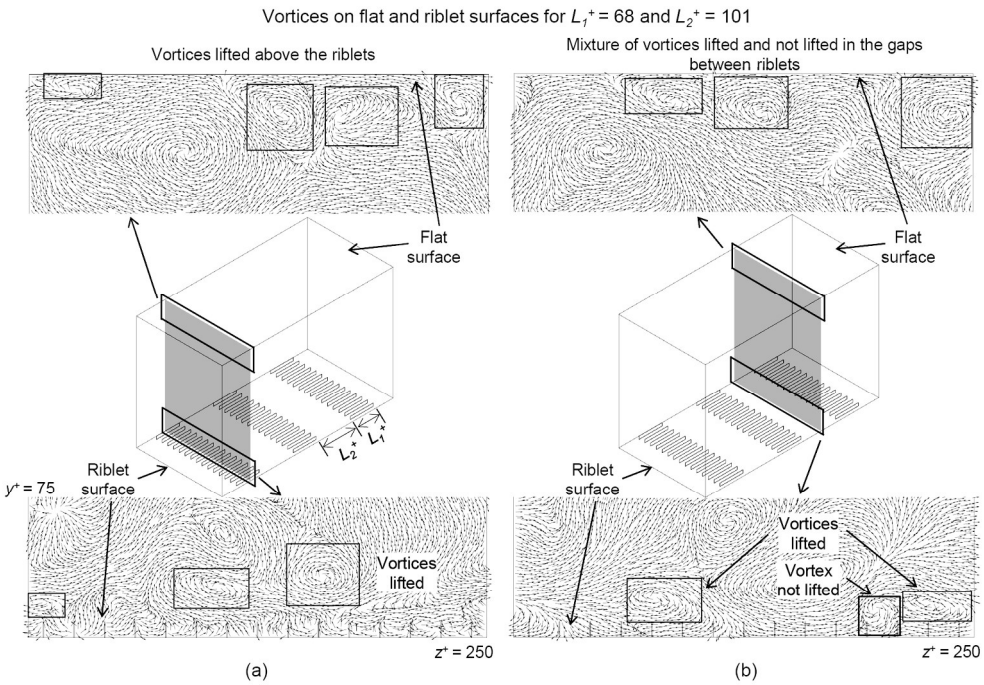

172x119mm (300 x 300 DPI)

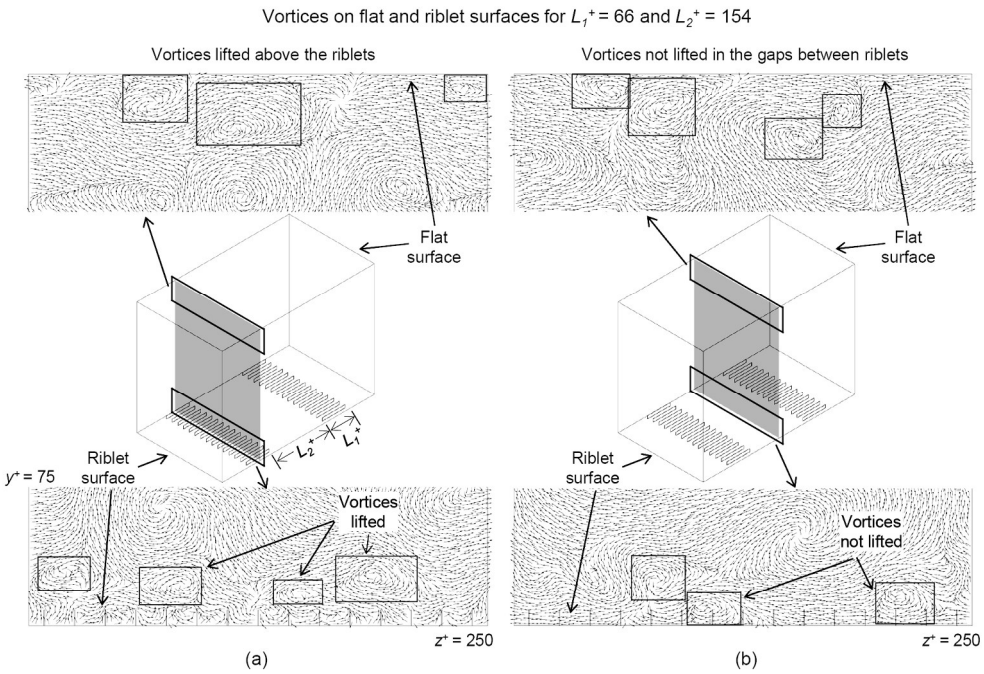

172x119mm (300 x 300 DPI)

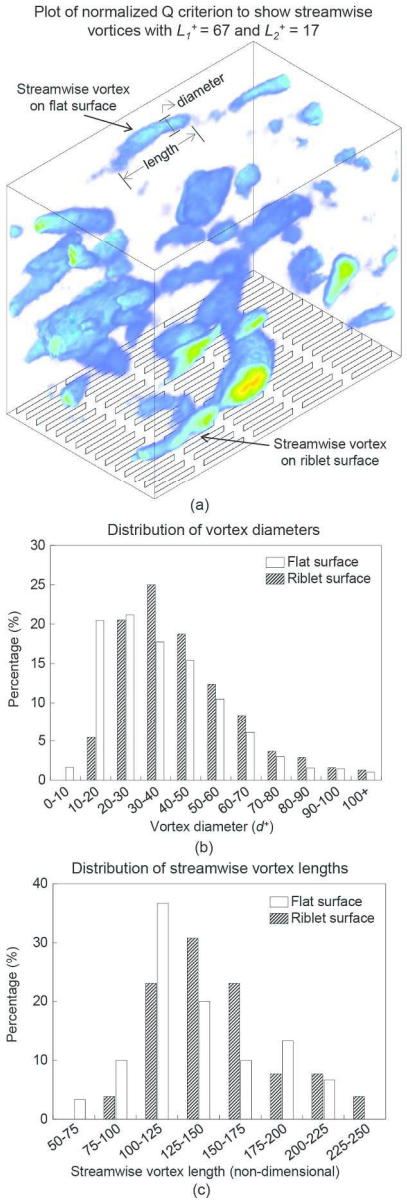

86x246mm (300 x 300 DPI)

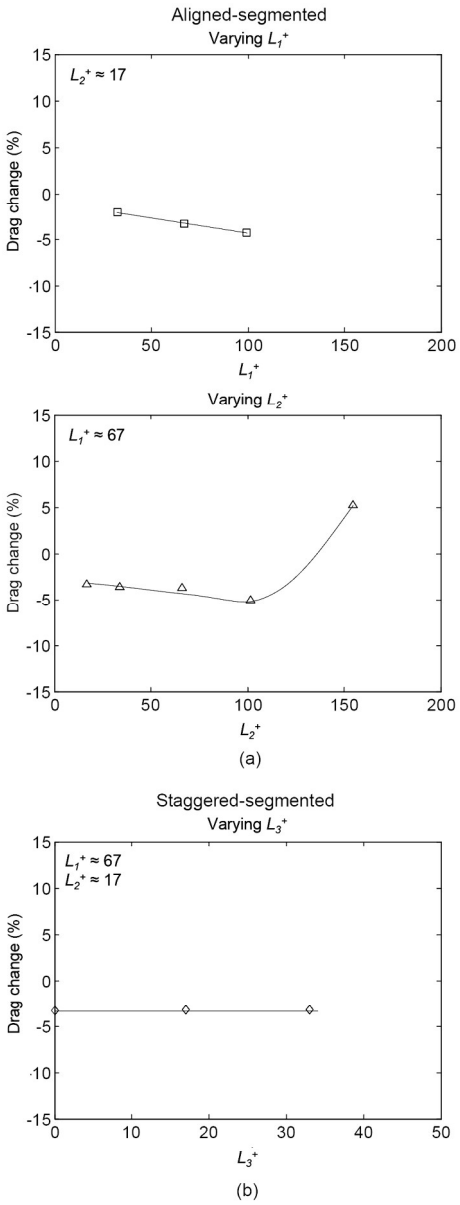

82x212mm (300 x 300 DPI)

Adequate spacing dimensions can lift vortices from a flat surface and lead to a drag reduction. Spacing that is too large can have vortices not lifted from the surface (shown using continuous riblets)

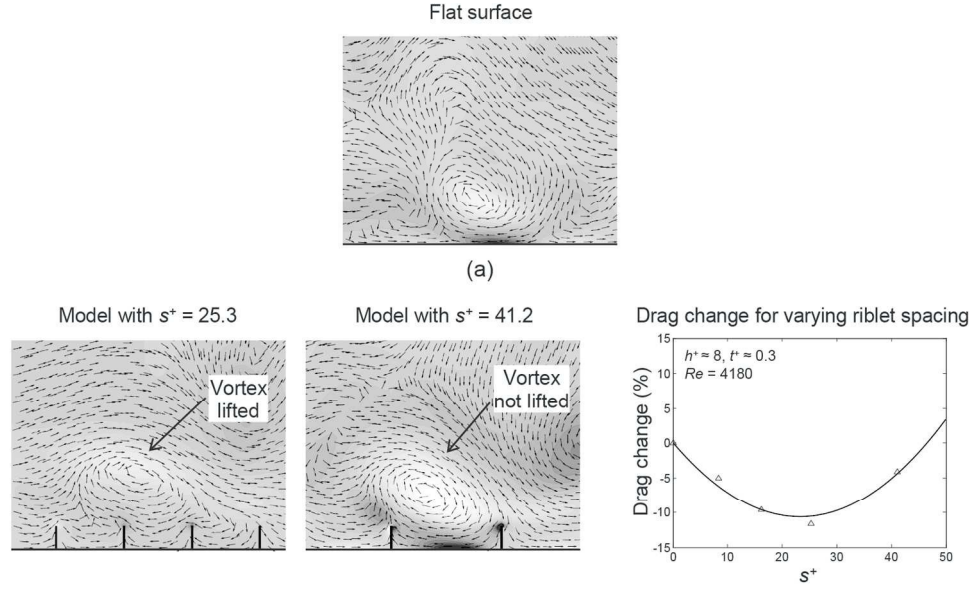

Adequate gap length can lift vortices from the surface (shown using aligned-segmented riblets)

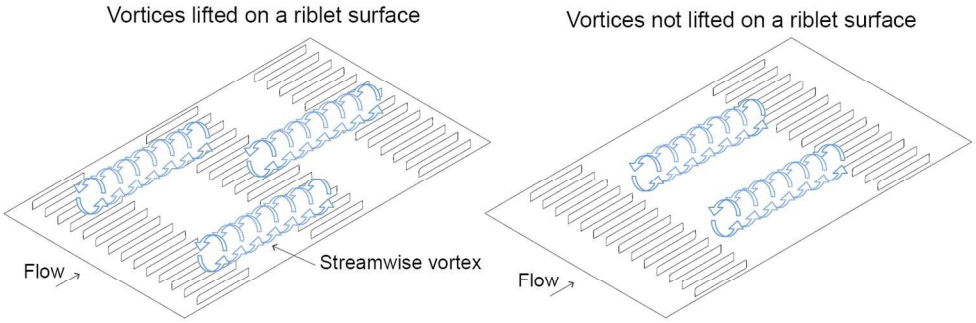

143x171mm (300 x 300 DPI)

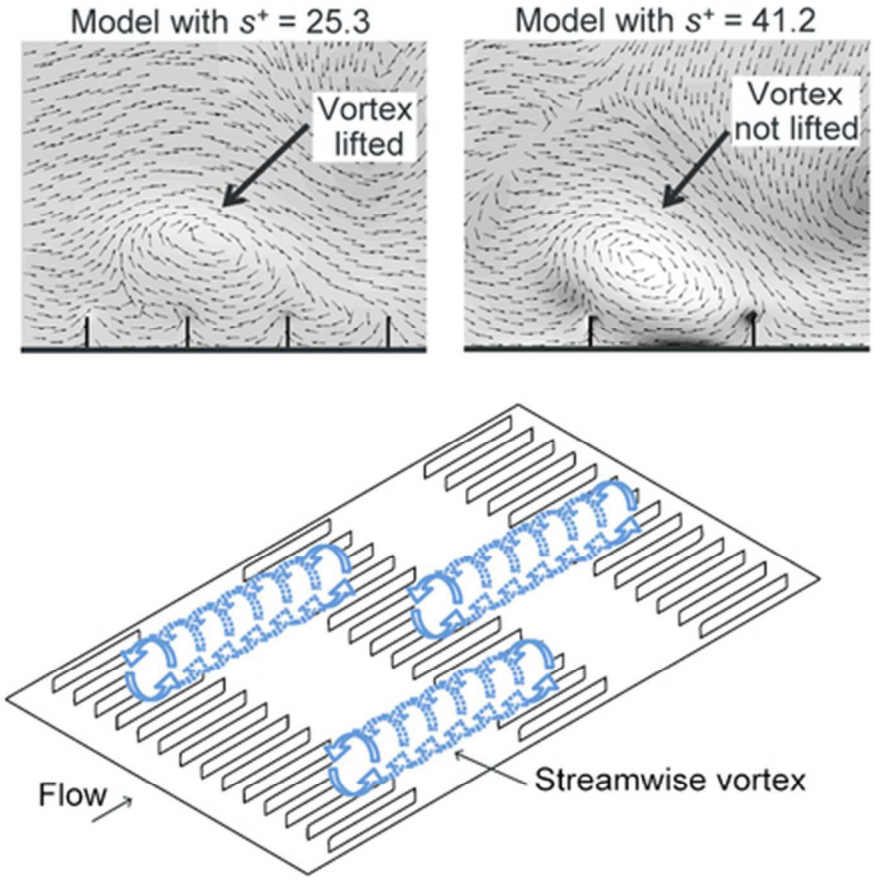

38x38mm (300 x 300 DPI)